SEISMIC CONSTRAINTS ON INTERIOR SOLAR CONVECTION

SHRAVAN M. HANASOGE[1,2], THOMAS L. DUVALL JR.[3], AND MARC L. DEROSA[4]
[1] Max-Planck-Institut für Sonnensystemforschung, Max Planck Straβe 2, 37191 Kaltenburg-Lindau, Germany; hanasoge@mps.mpg.de
[2] Department of Geosciences, Princeton University, Princeton, NJ 08544, USA
[3] Solar Physics Laboratory, NASA/Goddard Space Flight Center, Greenbelt, MD 20771, USA
[4] Lockheed Martin Solar and Astrophysics Laboratory, Palo Alto, CA 94304, USA

ABSTRACT

We constrain the velocity spectral distribution of global-scale solar convective cells at depth using techniques of local helioseismology. We calibrate the sensitivity of helioseismic waves to large-scale convective cells in the interior by analyzing simulations of waves propagating through a velocity snapshot of global solar convection via methods of time–distance helioseismology. Applying identical analysis techniques to observations of the Sun, we are able to bound from above the magnitudes of solar convective cells as a function of spatial convective scale. We find that convection at a depth of $r/R_\odot = 0.95$ with spatial extent $\ell < 20$, where ℓ is the spherical harmonic degree, comprises weak flow systems, on the order of 15 m s^{-1} or less. Convective features deeper than $r/R_\odot = 0.95$ are more difficult to image due to the rapidly decreasing sensitivity of helioseismic waves.

Key words: convection – hydrodynamics – Sun: helioseismology – Sun: interior – Sun: oscillations – waves

1. INTRODUCTION AND METHODOLOGY

Constraining the length scales and velocities of solar interior convection is an important step toward testing and improving models of astrophysical convection. In this regard, two observational efforts have received much attention: the detection of the elusive "giant cells" (e.g., Brown & Gilman 1984; Chiang et al. 1987; Wilson 1987; Beck et al. 1998; Featherstone et al. 2006) and a study of supergranulation and near-surface convection (e.g., Zhao & Kosovichev 2003; Woodard 2007). Despite these numerous investigations, neither have giant cells been conclusively observed, nor have the flow systems beneath supergranules been convincingly imaged. In particular, the inversions for supergranular flow are highly susceptible to the systematical issue of cross talk, a situation where different velocity components possess similar signatures in the observed time shifts. Questions relating to bounds on the degree of detectability of large-scale convection are also not new (e.g., van Ballegooijen 1986; Swisdak & Zweibel 1999; Hanasoge et al. 2007a).

The Anelastic Spherical Harmonic (ASH) simulations of solar convection in a spherical shell have provided us with a computational picture of the dynamical appearance, evolution, and disappearance of giant convective cells (Miesch et al. 2000). These simulations encompass a large fraction of the solar convection zone, spanning 0.7 $R_\odot$ to 0.98 $R_\odot$. Because of the large disparity of timescales between the upper and lower regions of the convection zone, Miesch et al. (2000) invoke the anelastic approximation (Gough 1969) to render the problem computationally tractable and to limit the computational cost. The anelastic formulation of the Navier–Stokes equations disallows acoustic waves; since it can only capture the dynamics that are subsonic, the domain of computation is truncated at 0.98 $R_\odot$ because the near-sonic and supersonic fluid motion contained within the near-photospheric layers of the Sun would not be realistically captured. In spite of the use of physically unrealistic boundary conditions (i.e., impenetrable walls at the upper and lower radial boundaries) and parameters (e.g., Prandtl, Rayleigh, and Reynolds numbers) that differ markedly from those describing the Sun, these models provide the best indications at present of what transpires in the solar convective interior.

Acoustic waves are our primary source of information about the optically thick solar interior. Therefore, in order to begin the task of understanding the influence of convection on the waves, we insonify the ASH simulations and characterize the impact of the convective velocities on the wave-field statistics. In order to accomplish this, we employ the forward modeling techniques of Hanasoge et al. (2006), who have devised a computational means of studying the impact of thermal and flow perturbations on the acoustic wave field. We place a velocity snapshot of the convection zone from an ASH calculation in a solar-like stratified background and simulate wave propagation through this complex medium (cf. Figures 1 and 2 of Miesch et al. 2008). We apply the method of time–distance helioseismology (Duvall et al. 1993), which primarily utilizes temporal correlations of velocity signals at spatially disparate points in order to construct the statistics of the wave field. In particular, we use the technique of deep focusing (Duvall et al. 2001), which relies on an elegant choice of observation points, leveraged in a manner so as to optimize the imaging capability, as illustrated in Figure 1. This method allows us to image the three components of the background velocity field, i.e., the latitudinal, longitudinal, and radial velocities.

2. CONVECTION SNAPSHOT AND WAVE CALCULATION

For purposes of discussion, we adopt a spherical coordinate system, using symbols r, λ, and ϕ to denote radius, latitude, and longitude, respectively. Slices at three radii corresponding to $r = 0.714R_\odot, 0.85R_\odot, 0.979R_\odot$ are extracted from an ASH simulation of solar spherical convection (Miesch et al. 2008). Each slice consists of 2048 × 1024 longitudes and latitudes respectively, with the highest spherical harmonic degree being $\ell_{ASH} = 683$. Note that the number of latitudes and the maximum spherical harmonic degree are chosen to satisfy the relation $n_{lat} \geqslant 3\ell_{ASH}/2$ in order that the simulation be stable against aliasing instabilities. We linearly interpolate between the three slices to obtain a smooth velocity field as a function of radius. The depth variation of the rms variations in the velocity components is plotted in Figure 2(a). In panel (b), we plot the maximum wavenumber of 3.5 mHz waves that penetrate
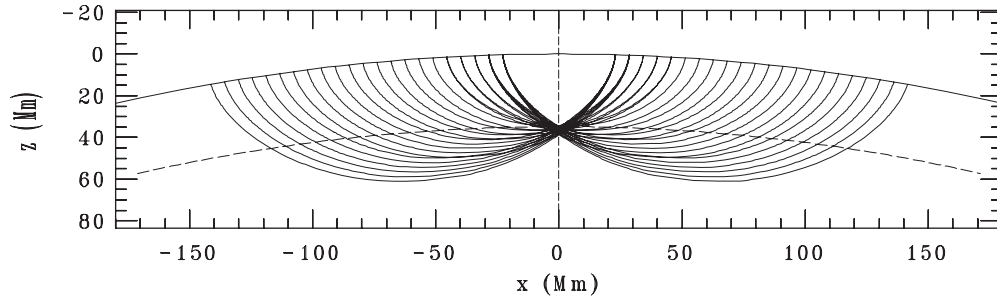
Figure 1. Pictorial representation of deep-focusing time–distance helioseismology. Numerous waves, denoted here by rays, that intersect at $r/R_\odot = 0.95$ are utilized in order to image flows at that depth (shown by the horizontal curved dashed line) and that horizontal location. The signal associated with the waves is measured at the solar photosphere (depicted by the horizontal curved solid line).
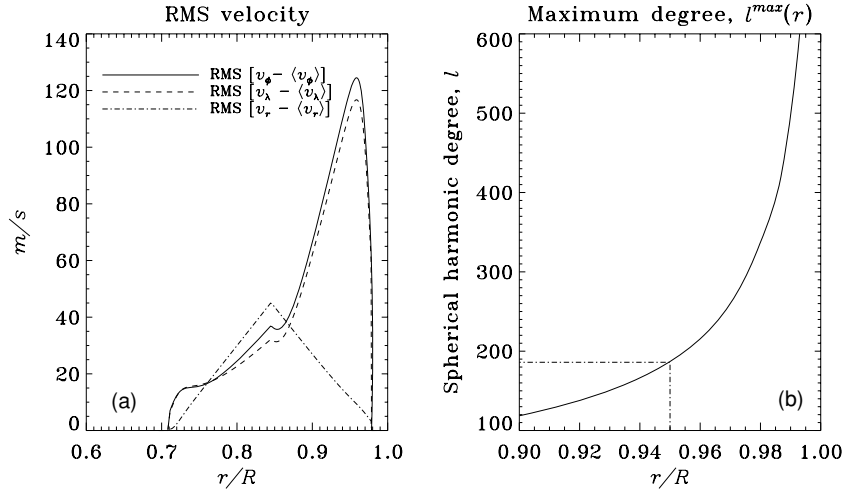
Figure 2. Velocity magnitude distribution of the three interpolated velocity components derived from the ASH simulation as a function of depth (panel (a)). Longitudinal averages of the components ($\langle v_\lambda \rangle$, $\langle v_\phi \rangle$) have been subtracted from horizontal velocities, lending the linearly interpolated rms profiles curvature (note: $v_r \approx 0$). The curve $\ell^{\max}(r)$ in panel (b) is the maximum wavenumber of 3.5 mHz waves that penetrate to that depth; because the imaging resolution is on the order of a wavelength, we are only able to image features that obey $\ell < \ell^{\max}(r)$; we also have $\ell^{\max}(r) \sim 185$ at $r/R_\odot = 0.95$.

a given depth (i.e., the inner turning points of the waves); this is roughly estimated as $\ell^{\max} = \omega r/c$, where ω is the angular frequency ($= 2\pi \times 0.0035$) of the waves and $c = c(r)$ is the sound speed. Because the imaging resolution is on the order of a wavelength (e.g., Gizon & Birch 2004), we are unable to detect convective features of scale $\ell > \ell^{\max}$ at that given depth. In the discussions that follow, we study the properties of convection at a depth $r/R_\odot = 0.95$, this layer being moderately distant from the upper boundary of the ASH simulations but not so deep that helioseismic analyses become noisy. From the curve in Figure 2(b), we determine that $\ell^{\max}(0.95R_\odot) \sim 185$, implying that convective features with $\ell > 185$ are not detectable at this depth. Thus, to moderate the computational cost, we filter the velocities in the spherical-harmonic domain so as to only retain wavenumbers $\ell < 256$ and then resample the data on to a grid of 768×384 longitudes and latitudes.

Having thus generated a three-dimensional cube of the convective velocities, we place it in a solar-like stratified spherical shell that extends from $r/R_\odot = 0.24$ to $r/R_\odot = 1.001$, and propagate waves through this medium according to the numerical recipe described in Hanasoge et al. (2006). We solve the three-dimensional linearized unsteady Euler equations describing wave propagation in spherical geometry in a temporally static background medium (in this case, the stratification and the convective velocities are constant in time). The waves are generated by deterministically forcing the radial momentum equation at a depth of approximately 100 km below the photosphere. Subsequently, a time series of the oscillation velocities

are extracted at a height of 200 km above the photosphere and used as artificial data for helioseismic investigations. We also apply the technique of noise subtraction (Hanasoge et al. 2007b) in order to obtain gains in the signal-to-noise ratio (S/N); two simulations are performed, one being a quiet calculation and the other with the convective velocity snapshot, both with identical source functions. The wave statistics of the former are subtracted from the latter, and the high degree of correlation between the two data sets results in a gain in the S/N and also a more direct view of the scattering process. Note that this is a luxury limited entirely to theoretical calculations and no observational analog exists (as yet).

3. TIME–DISTANCE ANALYSES AND CAVEATS

Time–distance measurements have primarily been made using cross-correlations connecting points with a common surface focus (Duvall et al. 1996). This is most appropriate for studying near-surface phenomena, although, as Giles (2000) has shown, it is possible to use that type of geometry to study very deep axisymmetric perturbations. A second type of geometry using cross-correlations from pairs of points at opposite sides of a circle (Duvall 2003) would seem to be more appropriate for focusing on deep phenomena, although different distances then have common points at different depths. In a slightly different technique, adopted by Rajaguru (2008), averages of signals over a quadrant of a circle are cross-correlated with the signals at the opposite quadrant. A possibly superior approach is to
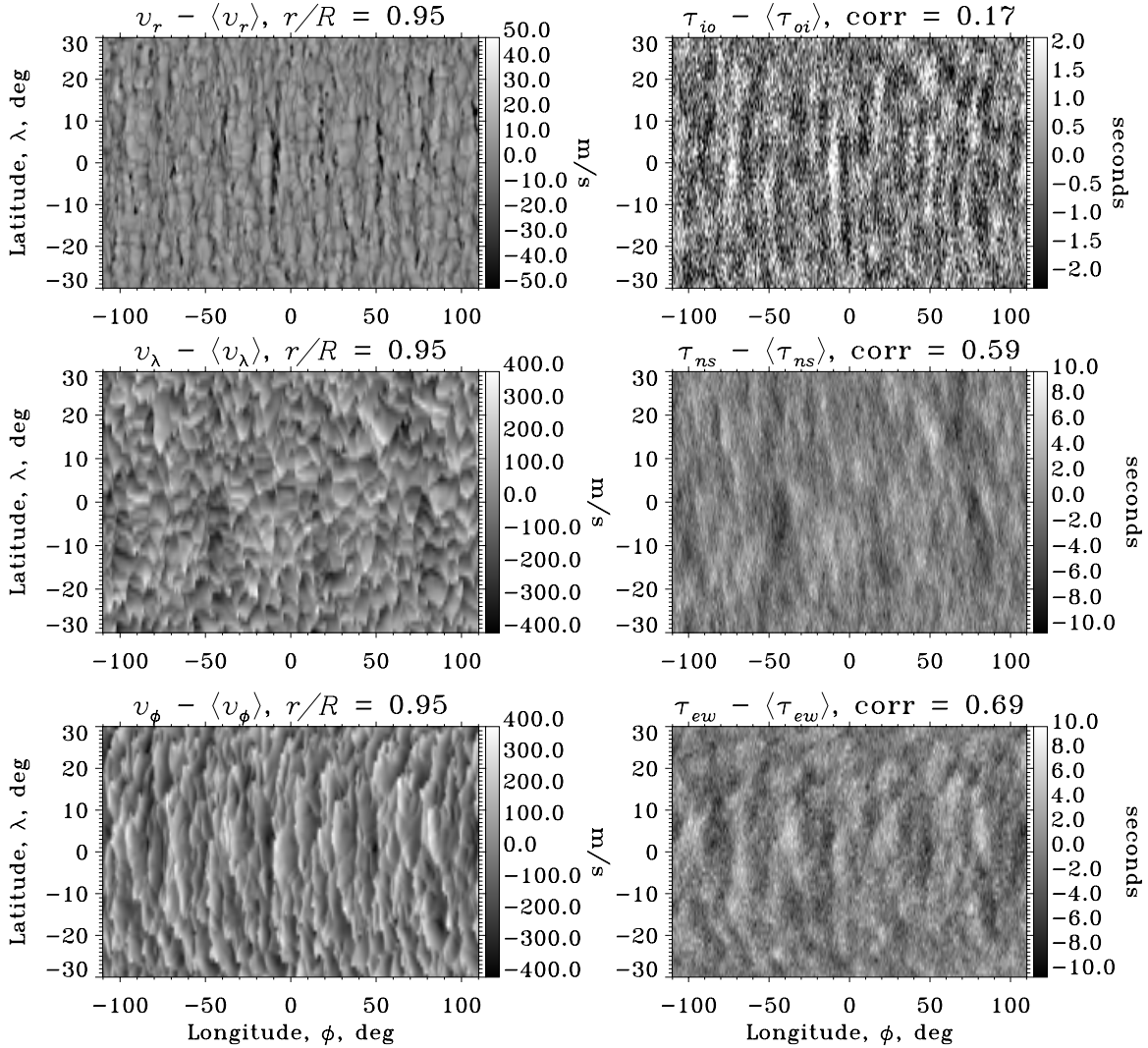
Figure 3. Comparison of flows at a depth of $r/R_\odot = 0.95$ and deep-focus travel-time differences (configuration shown in Figure 1). The left column shows the flows from the simulation: from top to bottom, the radial (v_r), north–south (v_λ), and east–west (v_ϕ) components at $r/R_\odot = 0.95$. Travel-time differences corresponding to these three components are shown on the right-hand column: from top to bottom, the difference between the ingoing and outgoing travel times (τ_{io}), the north–south travel-time asymmetry (τ_{ns}), and the east–west travel-time asymmetry (τ_{ew}). The correlation coefficients between the flows and travel-time maps are 0.17 for the radial, 0.59 for the north–south, and 0.69 for the east–west cases. The spatial cross-correlations between the travel-time and velocity maps have a FWHM of $9°$ for both the north–south and east–west cases.

cross-correlate a number of pairs of points whose connecting ray paths all converge at a subsurface focus (Duvall 1995). This method is computationally expensive and although it would appear to be ideal, it was shown by Duvall et al. (2001) that the Born sensitivity kernel corresponding to this geometry actually has a hollow sphere about the "focus" point. This is consistent with the banana-doughnut nature of the two-point kernel, with zero sensitivity along the classical ray path (Marquering et al. 1999; Birch & Kosovichev 2000).

In the present study, the latter form of deep focusing is used. At each point on the map, the input datacube is interpolated onto a spherical polar coordinate grid with the surface projection of the focus point placed at the north pole. The grid is computed in co-latitude from the pole (or focus point) to the largest angular distance needed for the computation. The resolution in co-latitude is the same as for the input data. The grid contains an equal number of longitudinal points at each latitude, making it easy to compute cross-correlations between pairs of points on opposite sides of the focus point at different colatitudes. A ray calculation determines which pairs of points are to be used in

order to focus on the desired subsurface location. The extent in co-latitude is restricted by requiring that the rays lie within $45°$ of the horizontal tangent plane at the focus depth. In effect, this limits the distance of the antennae from the focal point.

The three travel-time maps obtained subsequently can be interpreted to relate to the flows in the following manner: divergence time shift maps (τ_{io}) correspond to radial flows, north–south time-shift maps (τ_{ns}) correspond to latitudinal velocities (v_λ), and the east–west time-shift maps (τ_{ew}) correspond to longitudinal velocities (v_ϕ). As is seen in Figure 3, there is a significant resemblance between the convective velocities at depth and the associated deep-focusing time shifts. In particular, the correlation between the east–west time shifts and the longitudinal convective velocities is at the level of 70%; latitudinal velocities are also strongly correlated with the north–south time shifts, at the level of 60%. The radial flows, significantly weaker than the other components, do not register quite so well in the travel times.

We now calibrate the shifts in travel times directly to the convective velocities at the focus depth ($r/R_\odot = 0.95$) of the
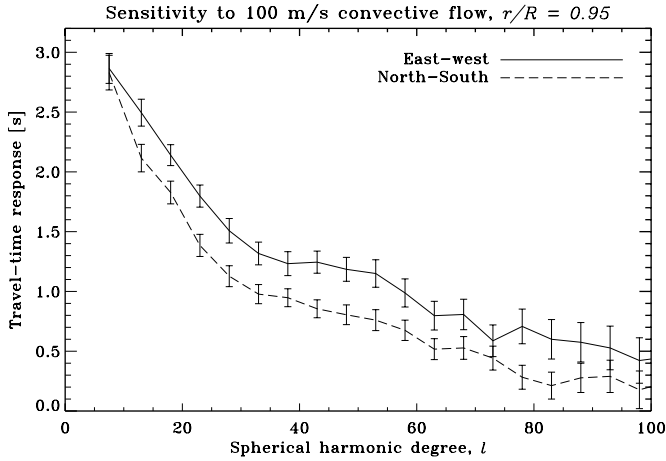
Figure 4. Measure of the imaging resolution of helioseismic waves. For example, a convective cell with horizontal velocity amplitude 100 m s^{-1} and dominant spatial power in $\ell = 1$ will elicit approximately a 3 s shift in the travel times as measured by this deep-focusing technique. Similar interpretations apply to convective features at higher ℓ. Finer-scale features at this depth, i.e., those characterized by $\ell > 50$, register much more weakly in the travel times. Note that these curves suggest an imaging resolution of $\ell \sim 30$ (defined as the half-width), far smaller than the largest wavenumber ($\ell^{\max} \sim 185$) that propagates at this depth ($r/R_\odot = 0.95$).

waves. We transform the velocities and time shifts into spherical harmonic space and perform a linear fit between the real and imaginary harmonic coefficients of the velocities and time shifts as a function of the bandpass (or spherical harmonic degree, ℓ). We graph this sensitivity in Figure 4. This calibration allows us to determine the induced time shift by a convective-cell-like feature at depth; thus, the observationally derived time shifts may be "inverted" in order to determine the convective velocity. A notable aspect of Figure 4 is that the imaging resolution (defined as the half-width) as indicated by the curves is $\ell \sim 30$, far smaller than $\ell^{\max} \sim 185$ at this depth ($r/R_\odot = 0.95$).

Caution must be exercised when interpreting this calibration process, primarily because the convection model we employ is greatly simplified and is likely not very comparable to the complex solar medium. In particular, we must keep in mind that (1) the sensitivity model of the waves has not been carefully investigated; thus, despite using this intricate focusing geometry, we possibly still retain considerable sensitivity to the near-surface layers (e.g., Figure 4.13 of Birch 2002); (2) we do not model the action of the near-surface convection on the waves, thereby not incorporating a significant source of wave scattering; (3) we linearly interpolate the convective velocity data in depth between the three available slices, thereby further reducing the complexity of the interior convection model; and (4) the solid-wall upper boundary condition applied in the ASH convection simulation leads to unrealistic convective velocity profiles, especially around $r/R_\odot = 0.979$.

4. OBSERVATIONS AND CONCLUSIONS

Deep-focusing analyses of individual days of quiet Sun Michelson Doppler Imager observations (MDI; Scherrer et al. 1995) show no indication of the presence of larger-scale convective features. The time shifts are dominated by noise. Furthermore, the correlation coefficient between time-shift maps of 1 day and the next (corrected for rotation) is too small to be regarded statistically significant. Similar to the work of Braun & Birch (2008), we utilize this non-detection to constrain the magnitudes of the convective velocities from above. We first obtain
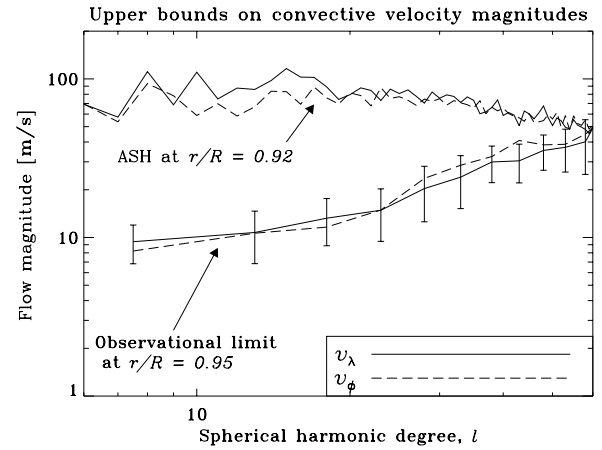
Figure 5. Upper bounds on the velocity magnitude spectrum of interior convection (with differential rotation and meridional circulation removed). Error bars are identical for both components, but for more clarity these are only shown for the longitudinal velocity. The average level of the travel-time noise in single day MDI medium-ℓ quiet Sun data is converted to velocity using the calibration curve in Figure 4. Based on the non-detection of convection, these form upper bounds on the velocities of convective cells. Giant cells with $\ell < 20$ at $r/R_\odot = 0.95$, if they exist, must therefore be of velocity magnitudes on the order of 15 m s^{-1} or less, making them very difficult to detect. Also plotted are spectra obtained from a 62 day average of the longitudinal and latitudinal convective velocities at $r/R_\odot = 0.92$ (Figures 13(b) and (c) of Miesch et al. 2008). Note that the velocity magnitude increases as a monotonic function of $r/R_\odot$, implying that the ASH velocity magnitudes are even higher at $r/R_\odot = 0.95$. Note that the seeming asymmetry in the error bars has to do with using a log scale.

estimates of the mean level of noise present in the travel times as a function of spherical harmonic degree. MDI medium-ℓ data from the two-year quiet period 2007 October–2009 October are analyzed and 28 synoptic charts of the travel times corresponding to as many Carrington rotation periods are constructed. Over a rotation period, a given heliocentric longitude is visible for 7 days; thus, the expectation noise level associated with the chart is $\sqrt{7}$ times the value derived from 1 day's analysis. We multiply the chart by this number in order to restore the noise to the 1 day level. The spherical harmonic spectra of these charts are then averaged, and a mean distribution of noise as a function of spherical harmonic degree is recovered. Lastly, these expectation values for the noise are divided by the calibration function of Figure 4 to obtain an upper-bound estimate for the convective velocities (Figure 5).

In other words, the noise-dominated time shifts are converted to velocities, with the implication that the magnitude of the interior solar convective velocity spectrum can be no greater than indicated by the curve in Figure 5, failing which large-scale convective cells become detectable within this observational window. As seen in the figure, the constraints place tight restrictions on the convective velocities, especially at low spherical harmonic degree. Giant cells at depth, if they exist, have small velocity magnitudes, on the order of 15 m s^{-1} or less, underscoring the remarkable challenge in actually detecting them. Also plotted is the longitudinal convective velocity spectrum obtained from a 62 day average of the ASH simulations; these velocities are seen to be of much greater magnitude than suggested by the observations. The 1σ error bars in Figure 5 are estimated by propagating the errors on the sensitivities (Figure 4) and the variance in the 1 day noise level. At each spherical harmonic degree ℓ, we average the noise associated with $2\ell + 1$ modes (i.e., $|m| \leqslant \ell$). Because very few modes are averaged at low ℓ, the primary source of uncertainty

in estimating the convective velocities is the (relatively) high degree of variance in the 1 day noise level. At higher spherical harmonic degrees, the sensitivity starts to fall and the associated uncertainties dominate.

REFERENCES

Beck, J. G., Duvall, T. L., Jr., & Scherrer, P. H. 1998, Nature, 394, 653
Birch, A. C. 2002, PhD thesis, Stanford Univ.
Birch, A. C., & Kosovichev, A. G. 2000, Sol. Phys., 192, 193
Braun, D. C., & Birch, A. C. 2008, ApJ, 689, L161
Brown, T. M., & Gilman, P. A. 1984, ApJ, 286, 804
Chiang, W.-H., Petro, L. D., & Foukal, P. V. 1987, Sol. Phys., 110, 129
Duvall, T. L., Jr. 1995, in ASP Conf. Ser. 76, GONG 1994. Helio- and Astro-Seismology from the Earth and Space, ed. R. K. Ulrich, E. J. Rhodes, Jr., & W. Dappen (San Francisco, CA: ASP), 465
Duvall, T. L., Jr. 2003, in Proc. SOHO 12/GONG+ 2002, Local and Global Helioseismology: the Present and Future, ed. H. Sawaya-Lacoste, (ESA SP-517; Noordwijk, Netherlands: ESA), 259
Duvall, T. L., Jr., Jefferies, S. M., Harvey, J. W., & Pomerantz, M. A. 1993, Nature, 362, 430
Duvall, T. L. J., D'Silva, S., Jefferies, S. M., Harvey, J. W., & Schou, J. 1996, Nature, 379, 235
Duvall, T. L., Jensen, J. M., Kosovichev, A. G., & Birch, A. C. 2001, AGU Spring Meeting Abstracts, 22
Featherstone, N. A., Haber, D. A., Hindman, B. W., & Toomre, J. 2006, in Proc. SOHO 18/GONG 2006/HELAS I, Beyond the Spherical Sun, ed. K. Fletcher & M. Thompson (ESA SP-624; Noordwijk, Netherlands: ESA), 133
Giles, P. M. 2000, PhD thesis, Stanford Univ.
Gizon, L., & Birch, A. C. 2004, ApJ, 614, 472
Gough, D. O. 1969, J. Atmos. Sci., 26, 448
Hanasoge, S. M., Duvall, T. L., Jr., & Couvidat, S. 2007a, ApJ, 664, 1234
Hanasoge, S. M., Duvall, T. L., Derosa, M. L., & Miesch, M. S. 2007b, in IAU Symp. 239, Convection in Astrophysics, ed. T. Kuroda, H. Sugama, R. Kanno, & M. Okamoto (Dordrecht: Kluwer), 364
Hanasoge, S. M., et al. 2006, ApJ, 648, 1268
Marquering, H., Dahlen, F. A., & Nolet, G. 1999, Geophys. J. Int., 137, 805
Miesch, M. S., Brun, A. S., De Rosa, M. L., & Toomre, J. 2008, ApJ, 673, 557
Miesch, M. S., Elliott, J. R., Toomre, J., Clune, T. L., Glatzmaier, G. A., & Gilman, P. A. 2000, ApJ, 532, 593
Rajaguru, S. P. 2008, arXiv:0802.2756
Scherrer, P. H., et al. 1995, Sol. Phys., 162, 129
Swisdak, M., & Zweibel, E. 1999, ApJ, 512, 442
van Ballegooijen, A. A. 1986, ApJ, 304, 828
Wilson, P. R. 1987, Sol. Phys., 110, 59
Woodard, M. F. 2007, ApJ, 668, 1189
Zhao, J., & Kosovichev, A. G. 2003, in Proc. SOHO 12/GONG+ 2002, Local and Global Helioseismology: the Present and Future, ed. H. Sawaya-Lacoste (ESA SP-517; Noordwijk, Netherlands: ESA), 417